1 # Trends of the high latitude mesosphere temperature and mesopause

2 # revealed by SABER

3 **Xiao Liu[1, 2], Jiyao Xu[2, 3], Jia Yue[4, 5], Yangkun Liu[1, 2], and Vania F. Andrioli[2, 6]**

4 [1]Institute of Electromagnetic Wave, School of Physics, Henan Normal University, Xinxiang,
5 453000, China

6 [2]State Key Laboratory of Space Weather, National Space Science Center, Chinese Academy of
7 Sciences, Beijing, 100190, China

8 [3]School of Astronomy and Space Science, University of the Chinese Academy of Science, Beijing,
9 100049, China

10 [4]Catholic University of America, Washington, DC 20064, USA

11 [5]NASA Goddard Space Flight Center, Greenbelt, MD, 20771, USA

12 [6]Heliophysics, Planetary Science and Aeronomy Division, National Institute for Space Research
13 (INPE), Sao Jose dos Campos, Sao Paulo, Brazil

15 *Correspondence to*: Jiyao Xu (xujy@nssc.ac.cn)

17 **Key Points:**

18 • The mean temperature in the high latitude MLT region is obtained by binning the SABER
19   observations based on yaw cycles during 2002–2023

20 • In the high latitude MLT, the cooling trend is seasonal symmetric and reaches peak of ≥6
21   K/decade at highest latitudes around summer solstice

22 • The trends of mesopause temperature depend on latitudes but are mostly negative and have
23   larger magnitudes at highest latitude

24

25

Abstract

The temperature trend in the mesosphere and lower thermosphere (MLT) region can be regarded as an indicator of climate change. Using temperature profiles measured by the Sounding of the Atmosphere using Broadband Emission Radiometry (SABER) instrument during 2002–2023 and binning them based on yaw cycle, we get continuous dataset with wide local time coverage at 50°S–80°N or 80°S–50°N. The seasonal change of temperature, caused by the forward drift of SABER yaw cycle, is removed by using the climatological temperature of MSIS2.0. The corrected temperature without any waves and is regarded as the mean temperature. At 50°S–50°N, the cooling trends of the mean temperature are significant in the MLT region and are in agreement with previous studies. The novel finding is that the cooling trends of ≥ 2 K/decade exhibit seasonal symmetric and reach peaks of ≥ 6 K/decade at highest latitudes around the summer solstice. Moreover, there are warming trends of 1–2.5 K/decade at pressure height range of 10^{-2}–10^{-3} hPa, specifically at latitudes higher than 55°N in October and December and at latitudes higher than 55°S in April and August. The mesopause temperature (height) in the northern summer polar region is colder (lower) than that in the southern counterpart by ~5–11 K (~1 km) over the past 22 years. The trends of the mesopause temperature are dependent on latitudes and months. But they are negative at most latitudes and reach larger magnitudes at highest latitudes. These results indicate that the temperature in high latitude MLT region is more sensitive to dynamic changes.

1   Introduction

Observational and simulation studies have revealed that the global mean temperature trend is cooling in the mesosphere and lower thermosphere (MLT) (Beig et al., 2003; Laštovička et al., 2006; Yue et al., 2019b; Laštovička, 2023). The cooling trends observed in the MLT region are mainly caused by the increasing anthropogenic greenhouse gases such as carbon dioxide. Moreover, changes of the stratospheric ozone depletion and recovery, increasing mesospheric water vapor concentration, solar and geomagnetic variations may also contribute to the long-term changes of temperature in the MLT region (Laštovička, 2009; Yue et al., 2019a, 2015; Garcia et al., 2019; Mlynczak et al., 2022; Zhang et al., 2023).

A recent review work by Laštovička (2023) summarized that temperature trends are generally cooling but also depend on local times, heights, and geographic locations in the MLT region (Venkat Ratnam et al., 2019; Das, 2021; She et al., 2019; Yuan et al., 2019; Ramesh et al., 2020). These results were mostly derived from ground-based and satellite observations at low and middle latitudes, while the simulations provided insights into the long-term trends from pole to pole. On the other hand, the long-term trends in temperature at high latitudes have not been thoroughly examined and well understood yet, due to scarce observations. Driven by the summer-to-winter meridional circulation, the upwelling causes adiabatic cooling in the summer polar mesosphere, while the downwelling causes adiabatic warming in the winter polar mesosphere (Dunkerton, 1978; Garcia and Solomon, 1985). Thus, the high latitude temperature is more sensitive to the changes of dynamics, wave and forcing, stratospheric wind etc. (Russell et al., 2009; Qian et al., 2017; Yu et al., 2023).

The progress in studying long-term trends in the MLT region has been summarized and reported by Laštovička and Jelínek (2019) and Laštovička (2023). Here we highlight some studies related to trends in temperature at high latitudes. Using temperature measured by the Sounding of the Atmosphere using Broadband Emission Radiometry (SABER) instrument and simulated by Whole Atmosphere Community Climate Model version 4 (WACCM4), Garcia et al. (2019) showed that the global mean SABER temperature (52°S–52°N) of a cooling trend of 0.4–0.5 K/decade during 2002–2018 in the stratosphere and mesosphere, were smaller than those simulated by WACCM4 (0.6–0.9 K/decade) but within 2 times of the standard deviation. Using Leibniz Institute Middle Atmosphere Model (LIMA) under northern hemispheric conditions during 1871–2008, Lübken et al. (2018) showed that the cooling trend in the MLT region was 1.5 K/decade during 1960–2008, and was 0.7 K/decade during 1871–2008 at 55–61°N on geometric heights. However, the trend was neglectable on pressure heights. On pressure heights, the global mean SABER temperature (55°S–55°N) had cooling trends of 0.5 and 2.6 K/decade, respectively, at 10^{-3} hPa (~92 km) and 10^{-4} hPa (~106 km) during 2002–2021 (Mlynczak et al., 2022). The results of Lübken et al.

80   (2018) and Mlynczak et al. (2022) illustrated that the cooling trends were larger over recent decades

81   on both geometric and pressure heights as compared to the beginning of industrialization. To

82   achieve a longer time series, Li et al. (2021) constructed a nearly 30-year dataset at 45°S–45°N by

83   merging the temperature measured by the Halogen Occultation Experiment (HALOE) instrument

84   during 1991–2005 and the SABER instrument during 2002–2019. They showed that the cooling

85   trend was significant and reached a peak of 1.2 K/decade at 60–70 km in the Southern Hemisphere

86   (SH) tropical and subtropical region. Moreover, the cooling trend in the SH was larger than its

87   counterpart in the Northern Hemisphere (NH).

88   At high latitudes, ground-based observations of OH nightglow rotational temperature revealed

89   a significant cooling trend of 1.2 ± 0.51 K/decade at Davis (68°S, 78°E) during 1995–2019 (French

90   et al., 2020). The OH rotational temperature around midnight exhibited a significant cooling trend

91   of 2.4 K± 2.3/decade in summer and an insignificant cooling trend of 0.4 ± 2.2K/decade in winter

92   at Moscow (57°N, 37°E) during 2000–2018 (Dalin et al., 2020). Using the ice layer parameters

93   simulated by the LIMA model and the Mesospheric Ice Microphysics And transport ice particle

94   model, Lübken et al. (2021) showed that the negative trend of noctilucent clouds heights (~83 km)

95   was primarily caused by CO_2-induced cooling at lower heights during 1871–2008 at 58°N, 69°N,

96   and 78°N. At these three latitudes, the cooling trends were of ~0.2 K/decade during 1871–1960 and

97   1.0 K/decade during 1960–2008. Near the latitude band of 64–70°N in June and 64–70°S in

98   December, Bailey et al. (2021) constructed two datasets by merging the temperature measured by

99   HALOE and SABER and by HALOE and SOFIE (Solar Occultation for Ice Experiment). They

100   showed that there were cooling trends of ~1–2 K/decade near 0.1–0.01 hPa (~68–80 km) and

101   warming trends of ~1 K/decade near 0.005 hPa (~85 km) at 64–70°N in June and 64–70°S in

102   December. Moreover, the WACCM-X simulation results by Qian et al. (2019) showed that the

103   temperature trends were mostly cooling in the MLT region. However, there were also warming at

104   ~80–95 km in the SH polar region from November to February (Fig. 3 of their paper). The

105   disagreement of these results at high latitudes might attribute to the different temporal spans and

106   local times, observations using different instruments, and different methods deriving the trends. It is

107   overarching to study the temperature trends at high latitudes using one coherent measurement over a

108   long period.

109   The SABER temperature profiles cover latitudes of 53°S–83°N in the north viewing

110   maneuvers and 83°S–53°N in the south viewing maneuvers since 2002. Each temperature profile

111   covers a height range of ~15–110 km with accuracies of ~1.8–2.3 K at z=60–80 km and ~5.4–8.4 K

112   at 90–100 km and vertical resolution of 2 km (Remsberg et al., 2008; Rezac et al., 2015). These data

113   exhibited remarkable stability over the last two decades following the correction of algorithm

114   instability (Mlynczak et al., 2020, 2022, 2023). Using the SABER temperature profiles during

115   2002–2019, Zhao et al. (2020) employed a 60-day moving window to obtain the mean temperature.

116   Their analysis revealed that the annual and global mean trend of mesopause temperature is cooling

117   with magnitude of 0.75 K/decade. Moreover, the cooling trend is significant in non-summer seasons

118   but insignificant in summer (May–August) at 60–80°N/S. It should be noted that, SABER yaw

119   cycle (YC) drifted forward about one month from 2002 to 2023 (see Fig. 1 below) due to changing

120   satellite orbit. This induces the local time (LT) coverage in a certain month differing from year to

121   year at high latitudes if the window is set to be constantly 60days.

122   Here we focus on the trend of the mean temperature without any atmospheric waves (i.e.,

123   gravity waves, tides and planetary waves). Calculating zonal mean can remove gravity waves,

124   nonmigrating tides and long-period planetary waves. However, migrating tides depend on LT and

125   are strong in the MLT region. They cannot be simply removed by calculating zonal mean. In this

126   work, we bin the data based on YC, which covers an interval of 54–64 days (see Fig. 1 below) and

127   provides almost full local time coverage (except the 1–3 hours around noon). Thus, the mean

128   temperature can be accurately determined by removing the migrating tides at 53°S–83°N or 83°S–

129   53°N using harmonic fitting. Each YC at every year covers varying ranges of dates. This results in

130   the aliasing of the seasonal variation of temperature into the mean temperature of each YC. This

131   issue can be resolved as below. We use the temperature of the recently released whole-atmosphere

132   empirical model MSIS2.0 (Emmert et al., 2021) as a reference for the seasonal variation. This

133   seasonal variation (more than 10 K as seen in Fig. 2b) embedded in YC drift is removed from the

134   mean temperature of each YC. Thus, using the advantages of SABER measurements at high

135   latitudes and binning the data based on YC, we focus on the long-term trends of the mean

136   temperature and the mesopause in the high latitude MLT region.

2   Method of calculating mean temperature and trend

138   The mean temperature ($\bar{T}_{bk}$) excludes gravity wave, tides and planetary waves. Moreover,

139   compared to the magnitudes of $\bar{T}_{bk}$, its trend is a small value and should be determined with extra

140   caution. The method of calculating $\bar{T}_{bk}$ is based on a YC window. This ensures a good LT coverage

141   at high latitudes. Compared to the fixed 60-day window, the advantage and necessity of the YC

142   window are described below.

143   The YC window is defined as the temporal interval during which the SABER measurements

144   are in the northward or southward viewing maneuver. Figure 1 shows the beginning date and

145   temporal span of each YC. We see that there are about six YCs in each year, being named as YC1–

146   YC6. The temporal spans of YCs are 54–64 days. This ensures that the LT coverage of SABER

147   samplings is more than 18 hours at high latitudes. Therefore, migrating tides can be removed

148   efficiently through harmonic fitting. In contrast, the LT coverage in a fixed 60-day window is

149   different from year to year at high latitudes. This is because the temporal span of each YC drifted

150   forward about one month from 2002 to 2023 (Fig. 1). For the case of the fixed 60-day window and

151   at 70°N and in March (spanning from 14th February to 14th April with a center on 15th March), the

152   sampling hours distributed at 0–2, 5–11, and 21–24 LT and had a coverage of only 14 hours in

153   2005. However, the sampling hours in 2022 distributed at 0–10 and 13–24 LT and had a coverage of

154   22 hours. The year-to-year variations of LT distribution and coverage might induce uncertainties

155   and biases into $\bar{T}_{bk}$. Thus, the YC dependent window is necessary to obtain a wide LT coverage.

156   We note that the forward drift of YC raises an issue that each YC at every year covers varying

157   ranges of date. This aliases seasonal variation of temperature into $\bar{T}_{bk}$ and should be removed to get

158   a corrected mean temperature ($\bar{T}_{bcrt}$). The detailed procedure of the calculating $\bar{T}_{bcrt}$ and its trend is

159   presented in Sec. 2.1–2.3. The procedure of calculating mesopause temperature and height is

160   presented in Sec. 2.4.

161
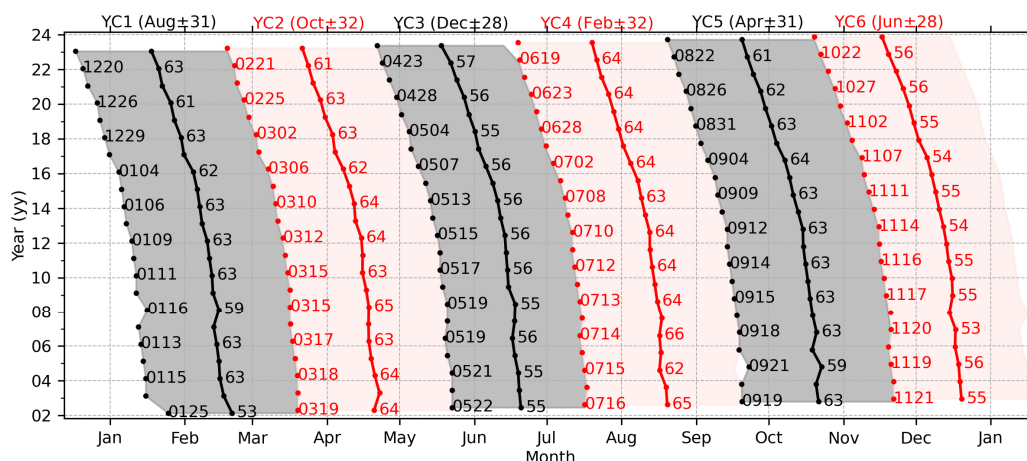
Figure 1. The temporal span of each YC from 2002 to 2023. The gray (red) region indicates the north (south) viewing maneuver. The beginning date (format of "mmdd", "mm" and "dd" mean the month and the day of month, respectively) and temporal span (unit of days) of each yaw are labeled on the right of beginning (dot) and center date (dot-line), respectively. The six YCs and their center date in 2003 and half spans and are labeled as YC1–YC6 on the top.

162

2.1   Removing waves from SABER temperature

164   In each YC, the background temperature is calculated at three steps. Firstly, at each latitude

165   band and pressure level, the daily zonal mean temperature ($\bar{T}_d$) is calculated by averaging the

166   temperature profiles at ascending and the descending nodes, respectively. This largely removes the

167   gravity waves, non-migrating tides, and long-period planetary waves. Here each latitude band has a

168 width of 10° with centers offset by 5° from 80°S to 80°N. Secondly, linear regression is performed

169 on $\bar{\bar{T}}_d$ at each node and is formulated as,

170
$$\bar{\bar{T}}_d = \bar{\bar{T}}_{d0} + kt_{UT}. \tag{1}$$

171 Here, $\bar{\bar{T}}_{d0}$ is the mean temperature in each YC. t_{UT} is the universal time with a unit of day, k

172 represents the linear variation of $\bar{\bar{T}}_d$ in each YC. After removing the linear variation (kt_{UT}) from

173 $\bar{\bar{T}}_d$, we get a residual temperature $\bar{\bar{T}}_{res}$ of each YC. Thirdly, tidal fitting is performed on $\bar{\bar{T}}_{res}$ of both

174 nodes and is formulated as,

175
$$\bar{\bar{T}}_{res} = \bar{\bar{T}}_{bk} + \sum_{n=1}^{3} a_n \cos(n\omega t_{LT} - \varphi_n). \tag{2}$$

176 Here, $\omega = 2\pi/24$ is the rotation frequency of Earth with a unit of rad/hour, t_{LT} is the local time

177 with a unit of hour, a_n and φ_n are, respectively, the amplitude and phase of migrating diurnal ($n =$

178 1), semidiurnal ($n = 2$) and terdiurnal ($n = 3$). Now, $\bar{\bar{T}}_{bk}$ excludes atmospheric waves and is

179 regarded as the mean temperature.

2.2 Removing seasonal variations from the mean temperature

181 Figure 1 shows that the center date of each YC shifts forward about one month from 2002 to

182 2023. This forward drift induces the seasonal variation of temperature into $\bar{\bar{T}}_{bk}$. This could further

183 alias the long-term trend calculated from $\bar{\bar{T}}_{bk}$ and can be removed with the help of MSIS2.0. This is

184 because MSIS2.0 has assimilated the SABER temperature profiles during 2002–2016. The

185 climatological temperature of MSIS2.0 coincides with that of SABER within the uncertainties of ~

186 3 K in the MLT region (Emmert et al., 2021). The detailed procedure of removing seasonal

187 variations is described below.

188 Firstly, we calculate the mean temperature of MSIS2.0. The temperature profiles (at 15

189 longitudes and 24 LTs each day) are calculated from MSIS2.0 under the conditions of lower solar

190 activity ($F_{10.7} = 50$ SFU) and geomagnetic quiet time ($ap = 4$ nT) throughout one calendar year.

191 Such that solar and geomagnetic activities do not influence the seasonal variation and trend of the

192 mean temperature. Then the daily zonal mean is performed on temperature profiles of each day.

193 This removes tides and long-period planetary waves. The daily zonal mean temperature in each YC

194 is averaged to get the mean temperature ($\bar{\bar{T}}_{MSIS}^{year}$, the superscript means the YC in that year). Figures

195 2(a1) and (a2) show the $\bar{\bar{T}}_{MSIS}^{year}$ at 70°N in YC3 and 70°S in YC6 during 2002–2023, respectively.

196 Secondly, we calculate the seasonal variations of each YC. The seasonal variations ($\Delta\bar{\bar{T}}_{MSIS}^{year}$)

197 caused by the forward drift of each YC in different years are quantified by the difference between

198 $\bar{\bar{T}}_{MSIS}^{year}$ of that year and the reference year (i.e., $\bar{\bar{T}}_{MSIS}^{2002}$). For example, the difference between 2003

199 and 2002 is calculated as $\Delta\bar{\bar{T}}_{MSIS}^{2003} = \bar{\bar{T}}_{MSIS}^{2003} - \bar{\bar{T}}_{MSIS}^{2002}$. More specifically, since $\bar{\bar{T}}_{MSIS}^{year}$ does not include

200 the year-to-year variations of temperature but depends on the temporal span of YC only, $\Delta\bar{\bar{T}}_{MSIS}^{2003}$ in

201 YC3 represents the seasonal variation from 20th to 19th June. Figures 3(b1) and (b2) show $\Delta\bar{\bar{T}}_{MSIS}^{year}$ at

202   70°N in YC3 and 70°S in YC6 during 2002–2023, respectively. It is evident that the forward drift of

203   YC induces temperature variations of ±20 K at 70°N/S from 2002 to 2023, and should be removed

204   before we determine the long-term trends in SABER temperature.

205
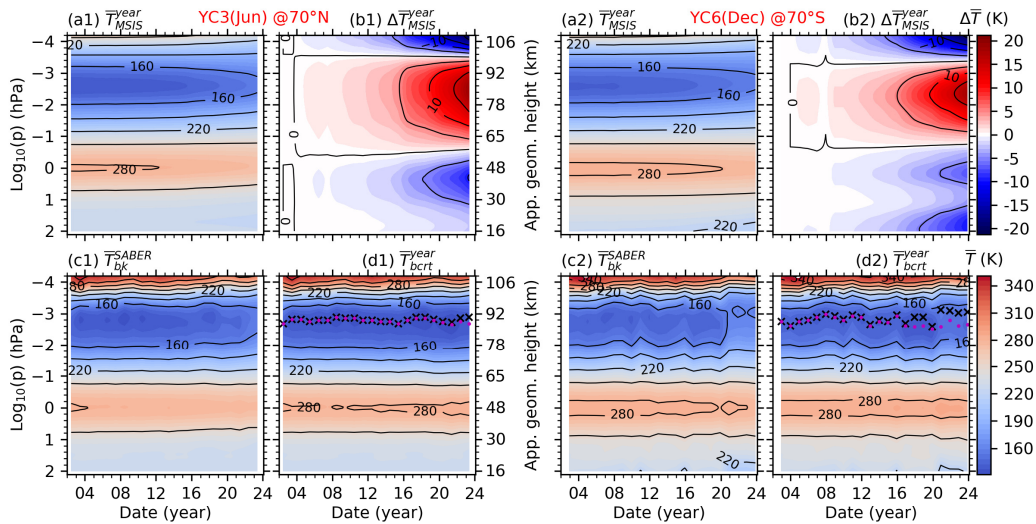
Figure 2. The date-height distributions of the mean temperature calculated from NRLMSIS 2.0 ($\overline{T}_{MSIS}^{year}$) and SABER ($\overline{T}_{bk}^{year}$) at 70°N in YC3 (left two columns) and 70°S in YC6 (right two columns). $\overline{T}_{MSIS}^{year}$ is used as a reference to calculate the seasonal variation ($\Delta\overline{T}_{MSIS}^{year}$) caused by the forward drift of YC from 2002 to 2023. Then, the corrected mean temperature ($\overline{T}_{bcrt}^{year}$) is calculated by removing $\Delta\overline{T}_{MSIS}^{year}$ from $\overline{T}_{bk}^{year}$. The mesopause heights calculated from $\overline{T}_{bk}^{year}$ and $\overline{T}_{bcrt}^{year}$ are plotted as black cross and red dots, respectively. The plots of $\overline{T}_{MSIS}^{year}$, $\overline{T}_{bk}^{year}$, and $\overline{T}_{bcrt}^{year}$ have the same colorbar of $\overline{T}$. The plot of $\Delta\overline{T}_{MSIS}^{year}$ has the colorbar of $\Delta\overline{T}$. Same scales in y-axis are used in all panels. The approximate geometric height is label on the right of the second column.

206

207   **Table 1.** The date range of each YC and its corresponding season in the reference year

YCs	YC1	YC2	YC3	YC4	YC5	YC6
Date range	20/Feb±31	20/Apr±32	20/Jun±28	19/Aug±32	13/Oct±31	10/Dec±28
Season	later winter	later spring	summer	early autumn	later autumn	winter

208

209   Finally, we correct the mean temperature. The corrected mean temperature ($\overline{T}_{bcrt}^{year}$, shown in

210   Figs. 3d1 and d2) is obtained by removing $\Delta\overline{T}_{MSIS}^{year}$ from $\overline{T}_{bk}^{year}$. This removes the seasonal variation

211   caused by the forward drift of YC from 2002 to 2023. Moreover, $\overline{T}_{bcrt}^{year}$ retains the long-term trend

212   of the mean temperature. We note that, after removing $\Delta\overline{T}_{MSIS}^{year}$, $\overline{T}_{bcrt}^{year}$ covered by each YC can be

213   represented by its center date and half span in the reference year (Tab. 1). Table 1 also lists the

214   approximate season related to each YC.

215

216   **2.3   Determining the long-term trend of the mean temperature**

217   To calculate accurate trends in the MLT region, multi-year variations should be removed

218   properly. The multi-year variations of temperature in the MLT region could be the solar cycle with a

219   period of about 11 years (Beig et al., 2008; Tapping, 2013; Forbes et al., 2014; Gan et al., 2017;

220   Qian et al., 2019), and the influences from below, such as the stratospheric quasi-biennial oscillation

221   (QBO) with a period of about 28 months (Baldwin et al., 2001; Zhao et al., 2021) and El Niño-

222   Southern Oscillation (ENSO) with varying cycles of around 2–7 years (Domeisen et al., 2019; Li et

223   al., 2013, 2016; Randel et al., 2009). The solar cycle can be represented by the solar radiation flux

224   at 10.7 cm (i.e., $F_{10.7}$ with unit of SFU=10^{-22}Wm^{-2}Hz^{-1}) (Tapping, 2013). ENSO is represented by

225   multivariate ENSO index (MEI) (Domeisen et al., 2019). QBO is represented by the monthly mean

226   zonal wind measured by radiosonde at Singapore (Baldwin et al., 2001). The multiple linear

227   regression (MLR) method is effective to separate the long-term trend in temperature from solar

228   cycle, ENSO and QBO. The MLR equation is formulated as,

229    $$Y(t) = c_0 + c_1 t + c_2 F_{10.7}(t) + c_3 \text{ENSO}(t) + c_4 \text{QBO}_{10}(t) + c_5 \text{QBO}_{30}(t) + \varepsilon(t). \quad (3)$$

230   Here, Y represents the mean temperature at year t from 2002 to 2023. c_0 represents a mean state of

231   Y. c_1 is the long-term trend of Y. c_2, c_3, c_4, c_5 represent the contributions from solar cycle, ENSO,

232   and QBO zonal wind at 10 hPa (QBO$_{10}$) and 30 hPa (QBO$_{30}$), respectively. The terms of $F_{10.7}$,

233   ENSO, QBO$_{10}$, and QBO$_{30}$ are included in Eq. (3) for the purpose of determining long-term trend

234   correctly but are not considered further in this work.

235   The statistical significances of the regression coefficients are measured by the student-t test

236   and the variance-covariance matrix of Eq. (3). Specifically, in Eq. (3), the sampling points are 22,

237   and the predictor variables are 6. This results in the degree of freedom of 16. Consequently, the

238   critical value is ~2.1 based on the student-t test at confidence level of 95% (Kutner et al., 2005).

239   This signifies that, with reference to the 95% confidence level, the magnitude of the regression

240   coefficient should be at least 2.1 times greater than the standard deviation.

241   **2.4   Determining the mesopause of each yaw cycle**

242   The mesopause temperature ($\bar{T}_{msp}$) is defined as the minimum of the mean temperature. The

243   pressure level where the minimum temperature occurs is defined as the mesopause height (z_{msp}).

244   Figures 2(d1) and (d2) show the mesopause heights calculated from $\bar{T}_{bk}^{year}$ (black cross) and $\bar{T}_{bcrt}^{year}$

245   (red dot), respectively. We see that the mesopause heights calculated from $\bar{T}_{bk}^{year}$ and $\bar{T}_{bcrt}^{year}$ are

246   nearly identical in the first several years but exhibit discrepancies over the later several years. This

247 implies that the seasonal variation caused by the forward drift of YC affects the mesopause heights

248 to some extent. Moreover, the mesopause heights exhibit larger variabilities in the southern summer

249 polar region (YC6) than that in the northern summer polar region (YC3). Figure 3 shows the date-

250 latitude distributions of the mesopause temperature ($\bar{T}_{msp}$) and height (z_{msp}) calculated from

251 $\bar{T}_{bcrt}^{year}$. We note that z_{msp} is defined on pressure level initially (Fig. 2d). To compare with previous

252 studies, z_{msp} is interpolated onto the geometric heights in Fig. 3.

253
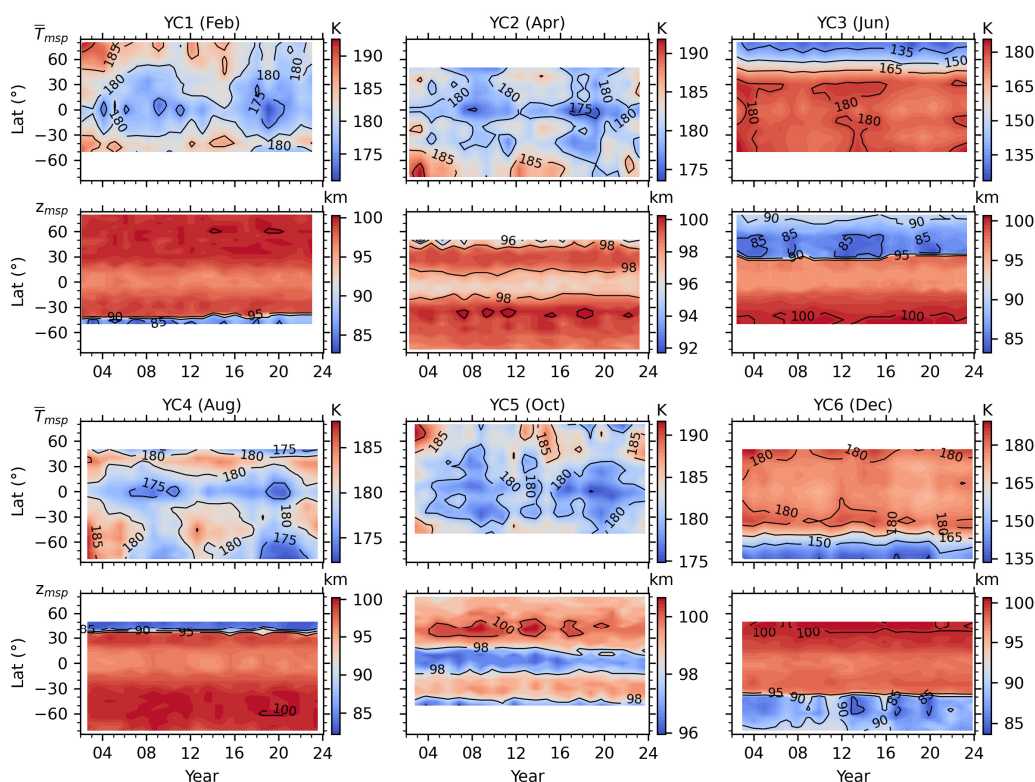
Figure 3. The date-latitude distributions of the mesopause temperature ($\bar{T}_{msp}$, the first and third rows) and height (z_{msp}, the second and fourth rows) calculated from $\bar{T}_{bcrt}^{year}$ of each YC from 2002 to 2023. Here z_{msp} is interpolated from pressure level to geometric height.

254

255 Previous SABER studies often discarded high latitudes possibly due to insufficient LT

256 coverage that induces uncertainties in the mean temperature estimation. A major advantage of

257 binning the SABER temperature based on YC is that an accurate mean temperature can be obtained.

258 Such that the latitude variations of $\bar{T}_{msp}$ and z_{msp} at high latitudes can be thoroughly studied.

259 Firstly, we focus on the YCs in northern summer and winter (i.e., YC3 and YC6) because the

260 summer mesopause at high latitudes is more sensitive to the summer-to-winter circulation

261   (Dunkerton, 1978; Qian et al., 2017). In YC3 (YC6), $\overline{T}_{msp}$ and z_{msp} decrease from 50°S to 80°N

262   (from 50°N to 80°S) in general. We note that $\overline{T}_{msp}$ has local minima around the Equator throughout

263   the 22 years in YC3 and YC6 and is the coldest at the highest latitudes of the summer hemisphere.

264   z_{msp} is the lowest at 40–60°N/S throughout the 22 years. Besides the latitude variations, $\overline{T}_{msp}$ and

265   z_{msp} also exhibit multi-year variations. For example, $\overline{T}_{msp}$ is colder around the Equator during the

266   solar minima (i.e., 2007–2008, 2019–2021) in YC3 and YC6. In YC6, the lower z_{msp} at the

267   southern higher latitudes might be related to the warm phase of ENSO during 2002–2005 and

268   2016–2019.

269   In YC2 and YC5, the latitude variations of $\overline{T}_{msp}$ and z_{msp} are almost hemispheric symmetry.

270    $\overline{T}_{msp}$ is the coldest around the Equator and the warmest at the highest latitudes. z_{msp} is the lowest

271   at lower latitudes and the highest at the highest latitudes. In YC1, $\overline{T}_{msp}$ and z_{msp} share the similar

272   latitude variations in winter (YC6). The difference is that $\overline{T}_{msp}$ is warmer in YC1 than that in YC6.

273   z_{msp} is higher in YC1 than that in YC6. In YC4, $\overline{T}_{msp}$ and z_{msp} share the similar latitude variations

274   in summer (YC3). The difference is that $\overline{T}_{msp}$ is warmer in YC4 than that in YC3. z_{msp} is higher in

275   YC4 than that in YC3. In YC1–2 and YC4–5, multi-year variations of $\overline{T}_{msp}$ exhibit clear solar cycle

276   dependence. At lower latitudes, $\overline{T}_{msp}$ are colder during the solar minima (i.e., 2006–2010, 2017–

277   2021). At high latitudes, $\overline{T}_{msp}$ are warmer during the solar maxima (i.e., 2002–2005, 2012–2014,

278   and after 2021). However, it looks like that the multi-year variations of z_{msp} are not as obvious as

279   those of $\overline{T}_{msp}$. These multi-year variations are considered in Eq. (3) to separate the long-term trend

280   in $\overline{T}_{msp}$ correctly but are not considered further in this work.

3   Trends of temperature in the MLT region and mesopause

3.1   Trends of temperature in the MLT region

283   Trends of the corrected mean temperature and their significances of each YC are shown in Fig.

284   4. These trends are generally larger at high latitudes than those at lower latitudes within the six YCs.

285   Moreover, the trends show both hemispheric symmetry and asymmetry approximately in the high

286   latitude MLT region.

287   First, we describe the hemispheric symmetry in the trends. In YC1 and YC4 and above 10^{-3}

288   hPa, the cooling trends are ≥2 K/decade at latitudes higher than 40°N (YC1) and 40°S (YC4),

289   respectively. Around 10^{-4} hPa, the cooling trends reach their peaks of ≥6 K/decade. In addition,

290   there are also warming trends of ≥2 K/decade at latitudes higher than 30°S (YC1) and 30°N (YC4),

291   respectively. Above mesopause, there are cooling trends of ≥2 K/decade observed within the latitude

292   range of 20–50°S for YC5 and 20–50°S for YC2. Additionally, in the region just below 10^{-3} hPa,

293   there are warming trends of ≥2 K/decade at latitudes of 50–80°N for YC5 and 50–80°S for YC2. In

294   YC3 and YC6, the cooling trends of ≥2 K/decade shift upward from the mesopause at 80°N (YC3)

295   and 80°S (YC6) to 10^{-4} hPa at 50°S (YC3) and 50°N (YC6). There are also cooling trends of ≥6

296   K/decade at high latitudes of summer hemisphere. Meanwhile, the coldest trends are ≥10 K/decade

297   just below 10^{-4} hPa and at 80°N/S. Although the cooling trends in the MLT region have been

298   reported extensively at lower and middle latitudes (Beig et al., 2003; Laštovička, 2023), the extreme

299   cooling trends at high latitudes and above the summer mesopause have not been reported yet.

300
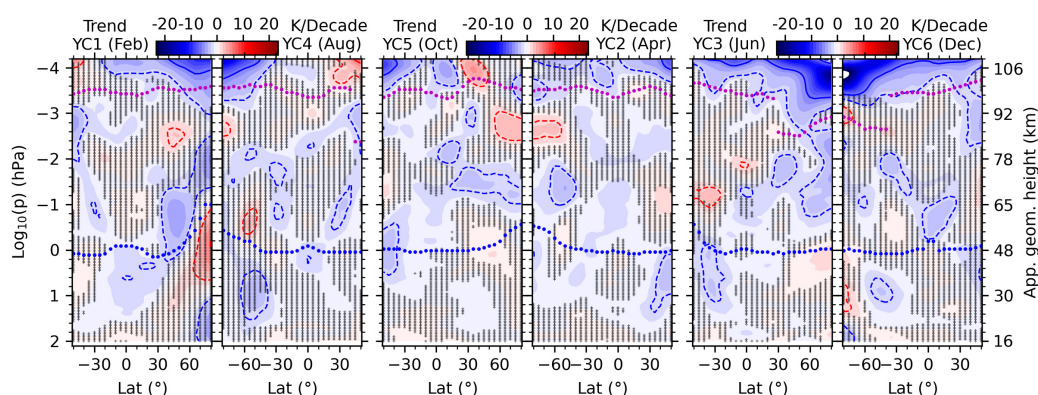
Figure 4. Trends of the corrected mean temperature in the six YCs. The solid and dashed contour lines indicate ±6 and ±2 K/decade, respectively. The red and green dots indicate the heights of the mesopause and stratopause, respectively. The regions marked by "+" indicate that trends are not significant with reference to the 95% the confidence level. The approximate geometric height is label on the last panel.

301

302   Next we describe the hemispheric asymmetry in the trends. In YC1 and YC4, the cooling

303   trends of ≥2 K/decade in YC1 extend to a wider latitude range (20°N–80°S) than those in YC4

304   (30°S–80°S) above 10^{-3} hPa. The insignificant warming trends of ≥2 K/decade can be seen in the

305   stratosphere at latitudes higher than 60°N in YC1 but at 45–60°S in YC4. In YC5 and YC2, the

306   cooling trends of ≥2 K/decade can be seen around the stratopause at 30–50°S (YC5) but below the

307   stratopause at 30–50°N (YC2). In YC3 and YC6, the significant warming trends of ≥2 K/decade in

308   YC6 are stronger than those in YC3 around 0.1 hPa. In addition, the warming trends near the

309   summer mesopause are significant in YC6 but insignificant in YC3. The simulation results in Qian

310   et al. (2019) also demonstrated warming trends in the southern summer MLT region. Specifically,

311   they showed significant warming trends below ~95 km and cooling trends above ~95 km at

312   latitudes exceeding 45°S between November and February. In contrast, there were insignificant or

313   warming trends at latitudes exceeding 45°N during June and July. Qian et al. (2019) attributed the

314   warming trend in the summer mesosphere to the changing meridional circulation.

3.2 Structure and trends of the mesopause

315

316   Taking advantages of the continuous measurements over a long-term (22 years or equivalently

317   two solar cycles), and YC binning at 50°S–80°N or 80°S–50°N, the robust mean states of the

318   mesopause temperature ($\bar{T}_{msp}$) and height (z_{msp}), as well as their trends and responses of $\bar{T}_{msp}$ to

319   solar cycle, ENSO, QBO are quantified using MLR. Here we focus on the mean states and trends of

320   the mesopause temperature and height.

321
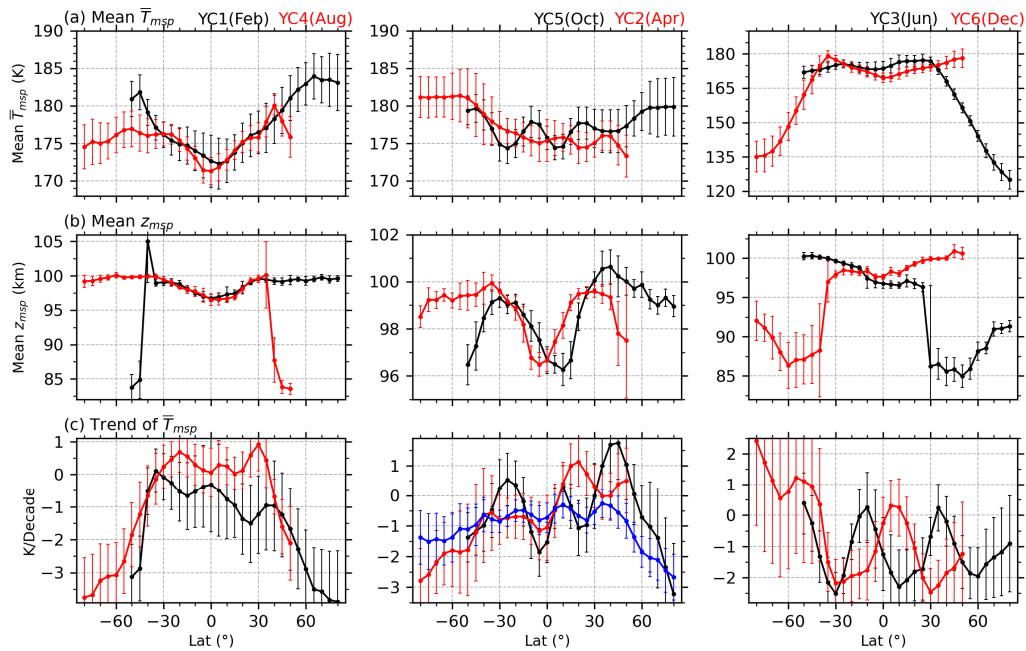
Figure 5. Latitude variations of the means of the mesopause temperature ($\bar{T}_{msp}$, a) and height (z_{msp}, b) and the trends of $\bar{T}_{msp}$ (c) of the six YCs. The error bar of each YC indicates 2.1 times standard deviation (i.e., at 95% confidence level according to the student-t test). The all-YC mean trend of mesopause temperature is shown as a blue line in the middle panel of (c).

322

323   Figures 5(a) and 7(b) show the mean $\bar{T}_{msp}$ and z_{msp} over 22 years of the six YCs. In YC1–2

324   and YC4–5, the mean $\bar{T}_{msp}$ is in the range of 172–183 K but is warmer at latitudes higher than 40°N

325   (YC1) and 40°S (YC2) those in the counterparts of YC4 and YC5. The mean z_{msp} is mainly in the

326   range of ~96–102 km but is higher than ~85 km at 40–50°N (YC1) and 40–50°N (YC4). In YC3,

327   the mean $\bar{T}_{msp}$ decreases sharply with latitudes from ~180 K at 30°N to ~125 K at 80°N. The mean

328   z_{msp} in YC3 reaches a minimum of ~85 km at 60°N. In YC6, the mean $\bar{T}_{msp}$ decreases sharply with

329   latitudes from ~180 K at 35°S to ~135 K at 80°S. The mean z_{msp} in YC6 reaches a minimum of

330 ~86 km at ~50°S. The mean $\bar{T}_{msp}$ (z_{msp}) in the northern summer polar region is colder (lower) than

331 that in the southern counterpart by ~5–11 K (~1 km). The hemispheric asymmetries of the summer

332 mesopause temperature and height coincide with Xu et al. (2007), who used the SABER

333 temperature data during 2002–2006 and showed that the mean $\bar{T}_{msp}$ in the summer polar region of

334 the NH is ~5–10 K colder than its counterpart in the SH. A recent study by Wang et al. (2022), who

335 used the SABER temperature data during 2002–2020, showed that the mean $\bar{T}_{msp}$ in the summer

336 polar region of the NH is ~10 K colder than its counterpart in the SH. Moreover, the transition

337 latitudes of the mean $\bar{T}_{msp}$ (z_{msp}) from higher temperature (height) are 30°N in YC3 and 40°S in

338 YC6. This coincides well with those reported by Xu et al. (2007) and Wang et al. (2022). These

339 hemispheric asymmetries of the mean $\bar{T}_{msp}$ and z_{msp}, and the transition latitudes could be caused

340 by the hemispheric asymmetry of solar radiation and gravity wave forcing (Xu et al., 2007).

341   Figure 5c shows that trends of $\bar{T}_{msp}$ in YC1 and YC4 are extreme cooling (≥2 K/decade) at

342 latitudes higher than 55°N/S. While at 40°S–40°N, trends of $\bar{T}_{msp}$ in YC1 are cooling with

343 magnitudes of ~0–2 K/decade but are warming in YC4 with magnitudes of ~0–1 K/decade. In YC2

344 and YC5, trends of $\bar{T}_{msp}$ are either cooling or warming, depending on the specific latitudes and

345 months being considered. At southern latitudes, trends of $\bar{T}_{msp}$ are cooling with magnitudes of ≥1

346 K/decade in YC2. Trends of $\bar{T}_{msp}$ in YC5 change sharply from 2.0 K/decade at 45°N to -3

347 K/decade at 80°N. In YC3 and YC6, trends of $\bar{T}_{msp}$ are mainly cooling except the insignificant

348 warming trends in YC6 and at latitudes higher than 40°S. Although trends of $\bar{T}_{msp}$ are warming at

349 some latitudes of certain YC, the all-YC mean trends of $\bar{T}_{msp}$ (blue line in Fig. 5c) are cooling with

350 magnitudes of 0.3–1 K/decade at 50°S–50°N. At latitudes higher than 55°S, the insignificant

351 cooling trends are ≤1.5 K/decade. In contrast, at latitudes higher than 55°N, the significant cooling

352 trends are ≥1.5 K/decade.

353 4   Discussions

354   Laštovička & Jelínek (2019) pointed out that the temporal interval of data might influence the

355 long-term trend. Using the nocturnal temperature in the MLT region measured by lidars around

356 41°N and 42°N over the period of 1990–2017, She et al. (2019) demonstrated that the cooling

357 trends are ~2.0–4.5 K/decade over only one solar cycle and are ~2.0–2.5 K/decade if the data

358 length is longer than two solar cycles. Using the SABER temperature profiles during 2002–2019,

359 Zhao et al. (2020) showed that the significant trends of $\bar{T}_{msp}$ and their responses to solar cycle can

360 be obtained at 50°S–50°N over longer than one solar cycle. Both She et al. (2019) and Zhao et al.

361 (2020) showed that the trends are relatively insensitive to the specific beginning and ending time of

362 the data as compared to the data length. Since the data length used in this study spans approximately

363 two solar cycles, the derived trends are highly reliable.

4.1   The reliability of trends in the MLT region

365 To facilitate a comparison with previously reported the annual and global-mean trends in the

366 MLT region, we present the mean trends of the corrected mean temperature at 50°S–50°N and at

367 55–80°S or 55–80°N of the six YCs (Fig. 6). The mean trends at 50°S–50°N of each YC are cooling

368 with magnitudes of ~0.5–1 K/decade at $10–10^{-3}$ hPa. The exception is the warming trend of 0.2

369 K/decade around 10^{-2} hPa in YC1 and of 0.1 K/decade around 4×10^{-3} hPa in YC3. At higher

370 heights, the cooling trends decrease sharply with height and reach to ~2 K/decade in YC5 and to ~3

371 K/decade in YC2 at 10^{-4} hPa. Compared to the situation in YC2 and YC5, the cooling trends

372 decrease more sharply with height in YC3 and YC6. Their magnitudes change nearly identically and

373 are from ~0.5 K/decade at 2×10^{-3} hPa to ≥5 K/decade at 10^{-4} hPa. When the mean trends at 50°S–

374 50°N across all-YC are further averaged, we obtain an annual mean trend (blue line in Fig. 5a). The

375 annual mean trend is cooling with magnitudes of ~0.5–0.8 K/decade and vary with height slightly at

376 $10–5\times10^{-4}$ hPa.

377 The height variation and the magnitude of the annual mean trend are similar to the previous

378 results (Garcia et al., 2019; Mlynczak et al., 2022; Zhao et al., 2021). Figure 3 of Garcia et al.

379 (2019) revealed that the global mean (52°S–52°N) SABER temperature trends are cooling with

380 magnitudes of ~0.5–0.9 K/decade at $10–5\times10^{-4}$ hPa during 2002–2018. These magnitudes are

381 slightly smaller than those derived from WACCM. Table 1 of Mlynczak et al. (2022) demonstrated

382 that the global mean (55°S–55°N) SABER temperature also display cooling trends with magnitudes

383 of ~0.51–0.63 K/decade at $1–10^{-3}$ hPa. Similarly, Fig. 4 of Zhao et al. (2021) revealed that the

384 global mean (50°S–50°N) SABER temperature trends are cooling with magnitudes of ~0.5–0.9

385 K/decade at 30–105 km. At 10^{-4} hPa, the extreme cooling trend of 2.6 K/decade in Table 1 of

386 Mlynczak et al. (2022) is smaller than the 5 K/decade derived here (blue line in Fig. 6a). Further

387 examming the trends across the six YCs (Figs. 4 and 6a), it becomes evident that the extreme

388 cooling trend is mainly attributed to the middle latitudes of summer hemisphere (i.e., YC3 and

389 YC6) and partially from other months. As suggested by Mlynczak et al. (2022), the extreme cooling

390 trend at 10^{-4} hPa is due to a decrease in solar irradiance that is not captured by the $F_{10.7}$ index.

391 These detailed comparisons showed that the trends at pressure levels reported by Garcia et al.

392 (2019) and Mlynczak et al. (2022) support the height varations and magnitudes of the trends derived

393 here directly. Although the trends reported by Zhao et al. (2021) are in geometric height, their

394 height varations and magnitudes agree with the trends derived here, too. Thus, the method of

395 binning SABER samplings based on YC leads a reliable global mean trends at 50°S–50°N.

396 Moreover, this method provides an opportunity to study the trends at latitudes higher than 55°N/S in

397 certain months.

398
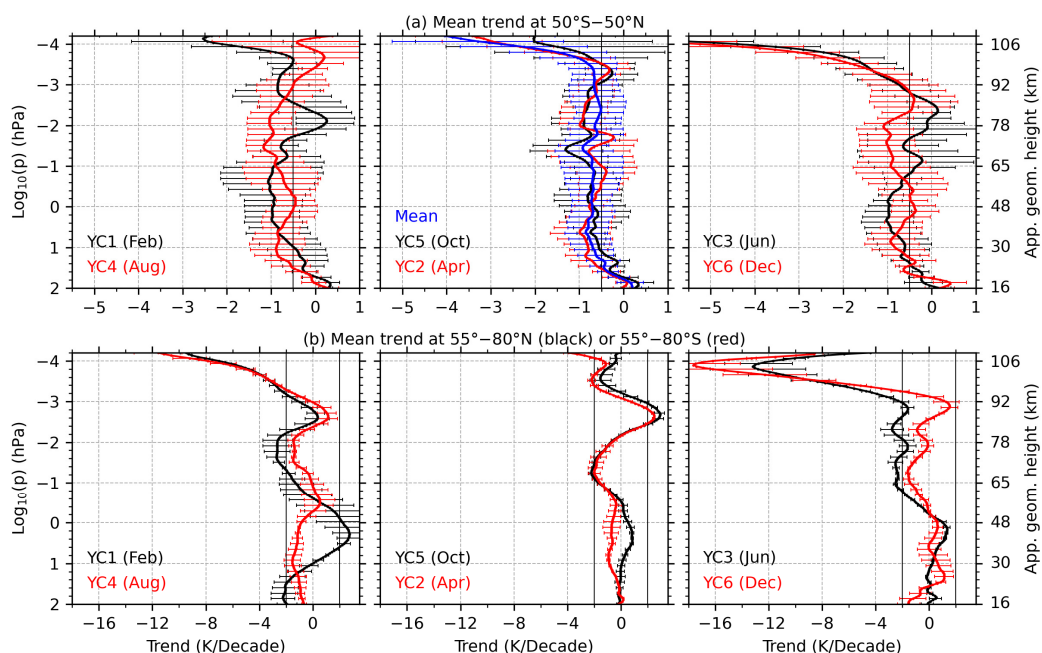
Figure 6. Mean trends of the corrected mean temperature at 50°S–50°N (a) and at 55–80°S (red line in b) or 55–80°N (black line in b) of the six YCs. The annual mean trend is calculated by averaging the trends of the six YCs at 50°S–50°N and is shown a blue line in the middle panel of (a). The error bars indicate standard errors of the averaged data.

399

At latitudes higher than 55°N/S, the height variations of the mean trends of the six YCs (Fig. 6b) are seasonal symmetric approximately above 1 hPa. The magnitudes of trends are mainly in the range of -2–2 K/decade below the height of 10^{-3} hPa. An interesting feature is the warming trends of 1–2.5 K/decade at 10^{-2}–10^{-3} hPa in April, August, October, and December. The peaks of the warming trends vary from 4×10^{-3} hPa to 10^{-3} hPa in different months. Focusing on the latitude band of 64–70°N in June and 64–70°S in December, Bailey et al. (2021) merged the temperature data form HALO and SABER (total length of 29 years) and HALOE and SOFIE (total length of 22 years). Their analysis revealed warming trends of 1–2 K/decade near 5×10^{-3} hPa (~85 km) at 64–70°N in June and 64–70°S in December, as illustrated in Fig. 7 of their paper. The results simulated by WACCM-X showed significant warming trends at ~80–95 km at latitudes higher than 45°S from November to February and close to zero or warming trends at latitudes higher than 45°N from June to July (Qian et al., 2019). The warming trends in December derived here coincides with those reported by Bailey et al. (2021) and Qian et al. (2019). The weak warming trend at 2×10^{-3} hPa in June coincides with those in Qian et al. (2021) but is much smaller than the 1–2 K/decade reported

414   by Bailey et al. (2021). In April and October, the warming trends are hemispheric symmetric at 10^{-2}–10^{-3} hPa and reach peak of ≥ 2 K/decade at 3×10^{-3} hPa. Above 10^{-3} hPa, the trends transit from warming to cooling.

417   The extreme cooling trends at high latitudes of the summer hemispheres (YC3 and YC6) might be resulted from the changing summer-to-winter circulation and gravity wave forcing in the MLT region. The circulation is upwelling in the summer hemisphere and causes a cold summer mesosphere through adiabatic cooling. Conversely, in the winter hemisphere, the circulation is downwelling, leading to a warm winter mesosphere through adiabatic warming (Garcia and Solomon, 1985). A necessary condition for the extreme cooling trends at summer high latitudes is the stronger upwelling and thus the increasing gravity wave body force in the summer hemispheres. Previous studies showed that the potential energy of gravity waves (GWPE) in the MLT region exhibited significant positive trends at southern high latitudes in January and at northern high latitudes in July (Fig. 5 of Liu et al., 2017). The positive trends of GWPE might enhance the strength of upwelling and thus the extreme cooling trends at high latitudes of summer hemispheres.

4.2   The reliability of the mesopause trends

429   The trends of $\bar{T}_{msp}$ derived in this study are significant and mainly negative at 50°S–50°N across most YCs. The averaged trend of $\bar{T}_{msp}$ of the six YCs is -0.64±0.22 K/decade over 50°S–50°N. When the average is performed over 80°S–80°N, the trend of $\bar{T}_{msp}$ of the six YCs is -1.03±0.40 K/decade. The cooling trend of $\bar{T}_{msp}$ derived here coincides also with the -0.5±0.21 K/decade in the mesosphere (Garcia et al., 2019) within only 50°S–50°N. Compared to the trend derived from sodium lidar observations during nighttime only around 40°N, the trends of $\bar{T}_{msp}$ from SABER are about -0.1, 0.0, -0.2, -0.8, 0.6, -1.9 K/decade in the six YCs and have annual mean of -0.4 K/decade. This is less than the significant cooling trend of 2.3–2.5 K/decade during 1990–2018 but is consistent with the insignificant cooling trend of 0.2–1 K/decade during 2000–2018 (Yuan et al., 2019). The comparisons of $\bar{T}_{msp}$ between our results and those from satellite, ground-based observations exhibit general consistencies in the sense of annual mean or global-mean.

440   A notable feature is the warming trends of $\bar{T}_{msp}$ with magnitudes of 0–2 K/decade at latitudes higher than 40°S in YC6. This warming trend is insignificant under 95% confidence level. If we change the temporal interval from 2002–2023 to 2002–2019, the trends of $\bar{T}_{msp}$ are cooling with magnitudes of 1–2 K/decade. Here we note that the year 2020 is just after the time when the SABER temperature data was revised (version 2.08, since 15 December 2019) (Mlynczak et al., 2023). In this work, we use the SABER temperature data of versions 2.07 (before 15 December 2019) and 2.08 (after 15 December 2019). According to Mlynczak et al. (2023), the new released data are free from the algorithm instability. On the other hand, there is no significant difference in

448   the counterpart of YC3. A recent study by Yu et al. (2023) showed that the Hunga Tonga Hunga-

449   Ha'apai (HTHH) volcanic eruption on 15 January 2022 induced temperature anomalies of ±10 K

450   globally in the stratosphere and mesosphere in August. The anomalies disappeared after September

451   2022. This indicates that the volcanic eruption may influence the mesosphere temperature through

452   circulations and waves. From the mesopause temperature of YC6 shown in Fig. 3, we see that the

453   warmer mesopause occurred after 2020 before the HTHH volcanic eruption. Thus, the largest

454   difference in YC6 may not be caused by the algorithm instability or the HTTH volcanic eruption but

455   a realistic result. As shown in Figs. 2(d) and 5(b) and reported by Wang et al. (2022), the annual

456   variability of z_{msp} is ~5 km at the southern high latitudes (YC6) but is relative stable at the northern

457   high latitudes (YC3). The large annual variability of z_{msp} induces a large variability of $\bar{T}_{msp}$

458   (indicated by large standard deviations in the right panel of Fig. 5b). This in turn contributes to the

459   large variability of the trends of $\bar{T}_{msp}$ at southern high latitudes.

5 Summary

461   Using the temperature profiles measured by the SABER instrument throughout the period of

462   2002–2023 (about two solar cycles) and binning them based on yaw cycles (YCs), we get

463   continuous data with good LT coverage within the range of 50°S–80°N or 80°S–50°N. Then we can

464   obtain an accurate mean temperature excluding atmospheric waves. The temporal span of each YC

465   drifted forward about one month from 2002 to 2023, aliasing the seasonal change in temperature

466   into long-term trends. This season change is removed by using the climatological temperature of

467   MSISE2.0. The remaining temperature is regarded as the corrected mean temperature ($\bar{T}_{bcrt}^{year}$) of

468   each YC. Then the mesopause temperature ($\bar{T}_{msp}$) and height ($\bar{z}_{msp}$) are calculated from $\bar{T}_{bcrt}^{year}$.

469   Such that the trends of the mean temperature and the mesopause structure can be studied in each YC

470   at high latitudes using MLR. The main results are summarized as below:

471   The cooling trends are significant in the MLT region and coincide well with previous results at

472   50°S–50°N. At latitudes higher than 55°N, the new findings are that the cooling trends have

473   magnitudes of ≥2 K/decade at northern high latitudes in February, April, and June and at southern

474   high latitudes in August, October, and December. There are also extreme cooling trends of ≥6

475   K/decade in the lower thermosphere at the northern highest latitude in February and June and at the

476   southern highest latitudes in August and December. Both the cooling and extreme cooling trends are

477   hemispheric and seasonal symmetric.

478   Besides the general cooling trends, there are also warming trends of 1–2.5 K/decade at 10^{-2}–10^{-3} hPa and at latitudes higher than 55°N in October and December and at latitudes higher than 55°S

480   in April and August. The peaks of the warming trends vary from 4×10^{-3} hPa to 10^{-3} hPa in different

481   months. The warming trend in December coincides with previous observational and simulation

482 results.

483   The mean $\bar{T}_{msp}$ (z_{msp}) in the northern summer polar region is colder (lower) than that in the

484 southern counterpart by a value of ~5–11 K (~1 km) over the past 22 years. Although the trends of

485 $\bar{T}_{msp}$ are highly dependent on latitudes and months, they are negative at most latitudes and have

486 larger magnitudes at higher latitudes. The trends of $\bar{T}_{msp}$ at the southern high latitudes in December

487 are highly dependent on the data length. The trends of $\bar{T}_{msp}$ change from warming of 0–2 K/decade

488 during 2002–2023 to cooling of 1–2 K/decade during 2002–2019. The significant dependence of the

489 trends of $\bar{T}_{msp}$ on the data length might be caused by the large annual variability of z_{msp} at the

490 southern high latitudes in December.

491   The trends of the mean temperature in the MLT region and mesopause are revealed from

492 continuous observations of the SABER instrument over the past 22 years. The data length is long

493 enough to determine reliable trends. Our results provide an observational proof that the extreme

494 cooling trends at high latitudes are more sensitive to the changing dynamics associated with climate

495 change and should be paid more attentions in future observational and model studies.

Author contributions

497   XL analyzed the data and prepared the paper with assistance from all co-authors. JX and JY

498 design the study. All authors reviewed and commented on the paper.

Data Availability Statement

500   All SABER data can be accessed from Space Physics Data Facility, Goddard Space Flight

501 Center (https://spdf.gsfc.nasa.gov/pub/data/timed/saber/ (last access: January 2024; Mlynczak et al.,

502 2023). The $F_{10.7}$ data were obtained from https://spdf.gsfc.nasa.gov/pub/data/omni/ (last access:

503 January 2024; Tapping, 2013). The QBO data were obtained from https://acd-

504 ext.gsfc.nasa.gov/Data_services/met/qbo/ (last access: January 2024; Baldwin et al., 2001). The

505 ENSO data were obtained from https://www.psl.noaa.gov/enso/mei/ (last access: January 2024;

506 Zhang et al., 2019; Wolter and Timlin, 2011)

Competing interests

508   The authors declare that they have no conflict of interest.

Acknowledgments

510   This work was supported by the National Natural Science Foundation of China (41874182,

511 42174196), the Project of Stable Support for Youth Team in Basic Research Field, CAS (YSBR-

512 018), the Informatization Plan of Chinese Academy of Sciences (CAS-WX2021PY-0101), and the

513 Open Research Project of Large Research Infrastructures of CAS "Study on the interaction between

514   low/mid-latitude atmosphere and ionosphere based on the Chinese Meridian Project". This work

515   was also supported in part by the Specialized Research Fund and the Open Research Program of the

516   State Key Laboratory of Space Weather.

References

518   Bailey, S. M., Thurairajah, B., Hervig, M. E., Siskind, D. E., Russell, J. M., and Gordley, L. L.: Trends in the polar
519   summer mesosphere temperature and pressure altitude from satellite observations, J. Atmos. Solar-Terrestrial
520   Phys., 220, 105650, https://doi.org/10.1016/j.jastp.2021.105650, 2021.

521   Baldwin, M. P., Gray, L. J., Dunkerton, T. J., Hamilton, K., Haynes, P. H., Randel, W. J., Holton, J. R., Alexander, M.
522   J., Hirota, I., Horinouchi, T., Jones, D. B. A., Kinnersley, J. S., Marquardt, C., Sato, K., and Takahashi, M.: The
523   quasi-biennial oscillation, Rev. Geophys., 39, 179–229, https://doi.org/10.1029/1999RG000073, 2001.

524   Beig, G., Keckhut, P., Lowe, R. P., Roble, R. G., Mlynczak, M. G., Scheer, J., Fomichev, V. I., Offermann, D., French,
525   W. J. R., Shepherd, M. G., Semenov, A. I., Remsberg, E. E., She, C. Y., Lübken, F. J., Bremer, J., Clemesha, B.
526   R., Stegman, J., Sigernes, F., and Fadnavis, S.: Review of mesospheric temperature trends, Rev. Geophys., 41,
527   https://doi.org/10.1029/2002RG000121, 2003.

528   Beig, G., Scheer, J., Mlynczak, M. G., and Keckhut, P.: Overview of the temperature response in the mesosphere and
529   lower thermosphere to solar activity, Rev. Geophys., 46, https://doi.org/10.1029/2007RG000236, 2008.

530   Dalin, P., Perminov, V., Pertsev, N., and Romejko, V.: Updated Long-Term Trends in Mesopause Temperature,
531   Airglow Emissions, and Noctilucent Clouds, J. Geophys. Res. Atmos., 125, 1–19,
532   https://doi.org/10.1029/2019JD030814, 2020.

533   Das, U.: Spatial variability in long-term temperature trends in the middle atmosphere from SABER/TIMED
534   observations, Adv. Sp. Res., 68, 2890–2903, https://doi.org/10.1016/j.asr.2021.05.014, 2021.

535   Domeisen, D. I. V., Garfinkel, C. I., and Butler, A. H.: The teleconnection of El Niño Southern Oscillation to the
536   stratosphere, Rev. Geophys., 57, 5–47, https://doi.org/10.1029/2018RG000596, 2019.

537   Dunkerton, T.: On the Mean Meridional Mass Motions of the Stratosphere and Mesosphere, J. Atmos. Sci., 35, 2325–
538   2333, https://doi.org/10.1175/1520-0469(1978)035<2325:OTMMMM>2.0.CO;2, 1978.

539   Emmert, J. T., Drob, D. P., Picone, J. M., Siskind, D. E., Jones, M., Mlynczak, M. G., Bernath, P. F., Chu, X.,
540   Doornbos, E., Funke, B., Goncharenko, L. P., Hervig, M. E., Schwartz, M. J., Sheese, P. E., Vargas, F., Williams,
541   B. P., and Yuan, T.: NRLMSIS 2.0: A Whole-Atmosphere Empirical Model of Temperature and Neutral Species
542   Densities, Earth Sp. Sci., 8, https://doi.org/10.1029/2020EA001321, 2021.

543   Forbes, J. M., Zhang, X., and Marsh, D. R.: Solar cycle dependence of middle atmosphere temperatures, J. Geophys.
544   Res. Atmos., 119, 9615–9625, https://doi.org/10.1002/2014JD021484, 2014.

545   French, W. J. R., Mulligan, F. J., and Klekociuk, A. R.: Analysis of 24 years of mesopause region OH rotational
546   temperature observations at Davis, Antarctica – Part 1: long-term trends, Atmos. Chem. Phys., 20, 6379–6394,
547   https://doi.org/10.5194/acp-20-6379-2020, 2020.

548   Gan, Q., Du, J., Fomichev, V. I., Ward, W. E., Beagley, S. R., Zhang, S., and Yue, J.: Temperature responses to the 11
549   year solar cycle in the mesosphere from the 31 year (1979–2010) extended Canadian Middle Atmosphere Model
550   simulations and a comparison with the 14 year (2002–2015) TIMED/SABER observations, J. Geophys. Res. Sp.
551   Phys., 122, 4801–4818, https://doi.org/10.1002/2016JA023564, 2017.

552   Garcia, R. R. and Solomon, S.: The effect of breaking gravity waves on the dynamics and chemical composition of the
553   mesosphere and lower thermosphere., J. Geophys. Res., 90, 3850–3868,
554   https://doi.org/10.1029/JD090iD02p03850, 1985.

555   Garcia, R. R., Yue, J., and Russell, J. M.: Middle atmosphere temperature trends in the twentieth and twenty-First
556   centuries simulated with the Whole Atmosphere Community Climate Model (WACCM), J. Geophys. Res. Sp.
557   Phys., 124, 7984–7993, https://doi.org/10.1029/2019JA026909, 2019.

558 Kutner, M., Neter, C. N. J., and Li, W.: Applied Linear Statistical Models, 5th ed., McGraw-Hill Irwin, Boston, 1396
559   pp., 2005.
560 Laštovička, J.: Global pattern of trends in the upper atmosphere and ionosphere: Recent progress, J. Atmos. Solar-
561   Terrestrial Phys., 71, 1514–1528, https://doi.org/10.1016/j.jastp.2009.01.010, 2009.
562 Laštovička, J.: Progress in investigating long-term trends in the mesosphere, thermosphere, and ionosphere, Atmos.
563   Chem. Phys., 23, 5783–5800, https://doi.org/10.5194/acp-23-5783-2023, 2023.
564 Laštovička, J. and Jelínek, Š.: Problems in calculating long-term trends in the upper atmosphere, J. Atmos. Solar-
565   Terrestrial Phys., 189, 80–86, https://doi.org/10.1016/j.jastp.2019.04.011, 2019.
566 Laštovička, J., Akmaev, R. A., Beig, G., Bremer, J., and Emmert, J. T.: Global Change in the Upper Atmosphere,
567   Science (80-.)., 314, 1253–1254, https://doi.org/10.1126/science.1135134, 2006.
568 Li, T., Calvo, N., Yue, J., Dou, X., Russell, J. M., Mlynczak, M. G., She, C. Y., and Xue, X.: Influence of El Niño-
569   Southern oscillation in the mesosphere, Geophys. Res. Lett., 40, 3292–3296, https://doi.org/10.1002/grl.50598,
570   2013.
571 Li, T., Calvo, N., Yue, J., Russell, J. M., Smith, A. K., Mlynczak, M. G., Chandran, A., Dou, X., and Liu, A. Z.:
572   Southern Hemisphere summer mesopause responses to El Niño-Southern Oscillation, J. Clim., 29, 6319–6328,
573   https://doi.org/10.1175/JCLI-D-15-0816.1, 2016.
574 Li, T., Yue, J., Russell, J. M., and Zhang, X.: Long-term trend and solar cycle in the middle atmosphere temperature
575   revealed from merged HALOE and SABER datasets, J. Atmos. Solar-Terrestrial Phys., 212, 105506,
576   https://doi.org/10.1016/j.jastp.2020.105506, 2021.
577 Liu, X., Yue, J., Xu, J., Garcia, R. R., Russell, J. M., Mlynczak, M., Wu, D. L., and Nakamura, T.: Variations of global
578   gravity waves derived from 14 years of SABER temperature observations, J. Geophys. Res., 122, 6231–6249,
579   https://doi.org/10.1002/2017JD026604, 2017.
580 Lübken, F. J., Berger, U., and Baumgarten, G.: On the Anthropogenic Impact on Long-Term Evolution of Noctilucent
581   Clouds, Geophys. Res. Lett., 45, 6681–6689, https://doi.org/10.1029/2018GL077719, 2018.
582 Lübken, F. J., Baumgarten, G., and Berger, U.: Long term trends of mesopheric ice layers: A model study, J. Atmos.
583   Solar-Terrestrial Phys., 214, 105378, https://doi.org/10.1016/j.jastp.2020.105378, 2021.
584 Mlynczak, M. G., Daniels, T., Hunt, L. A., Yue, J., Marshall, B. T., Russell, J. M., Remsberg, E. E., Tansock, J., Esplin,
585   R., Jensen, M., Shumway, A., Gordley, L., and Yee, J. H.: Radiometric Stability of the SABER Instrument, Earth
586   Sp. Sci., 7, 1–8, https://doi.org/10.1029/2019EA001011, 2020.
587 Mlynczak, M. G., Hunt, L. A., Garcia, R. R., Harvey, V. L., Marshall, B. T., Yue, J., Mertens, C. J., and Russell, J. M.:
588   Cooling and Contraction of the Mesosphere and Lower Thermosphere From 2002 to 2021, J. Geophys. Res.
589   Atmos., 127, 1–17, https://doi.org/10.1029/2022JD036767, 2022.
590 Mlynczak, M. G., Marshall, B. T., Garcia, R. R., Hunt, L., Yue, J., Harvey, V. L., Lopez-Puertas, M., Mertens, C., and
591   Russell, J.: Algorithm stability and the long-term geospace data record from TIMED/SABER, Geophys. Res. Lett.,
592   50, 1–7, https://doi.org/10.1029/2022GL102398, 2023.
593 Qian, L., Burns, A., and Yue, J.: Evidence of the Lower Thermospheric Winter-to-Summer Circulation From SABER
594   CO2 Observations, Geophys. Res. Lett., 44, 10,100-10,107, https://doi.org/10.1002/2017GL075643, 2017.
595 Qian, L., Jacobi, C., and McInerney, J.: Trends and solar irradiance effects in the mesosphere, J. Geophys. Res. Sp.
596   Phys., 124, 1343–1360, https://doi.org/10.1029/2018JA026367, 2019.
597 Ramesh, K., Smith, A. K., Garcia, R. R., Marsh, D. R., Sridharan, S., and Kishore Kumar, K.: Long-term variability and
598   tendencies in middle atmosphere temperature and zonal wind from WACCM6 simulations during 1850–2014, J.
599   Geophys. Res. Atmos., 125, https://doi.org/10.1029/2020JD033579, 2020.
600 Randel, W. J., Garcia, R. R., Calvo, N., and Marsh, D.: ENSO influence on zonal mean temperature and ozone in the
601   tropical lower stratosphere, Geophys. Res. Lett., 36, n/a-n/a, https://doi.org/10.1029/2009GL039343, 2009.
602 Remsberg, E. E., Marshall, B. T., Garcia-Comas, M., Krueger, D., Lingenfelser, G. S., Martin-Torres, J., Mlynczak, M.
603   G., Russell, J. M., Smith, A. K., Zhao, Y., Brown, C., Gordley, L. L., Lopez-Gonzalez, M. J., Lopez-Puertas, M.,

She, C. Y., Taylor, M. J., and Thompson, R. E.: Assessment of the quality of the version 1.07 temperature-versus-pressure profiles of the middle atmosphere from TIMED/SABER, J. Geophys. Res. Atmos., 113, 1–27, https://doi.org/10.1029/2008JD010013, 2008.

Rezac, L., Kutepov, A., Russell, J. M., Feofilov, A. G., Yue, J., and Goldberg, R. A.: Simultaneous retrieval of T(p) and CO2 VMR from two-channel non-LTE limb radiances and application to daytime SABER/TIMED measurements, J. Atmos. Solar-Terrestrial Phys., 130–131, 23–42, https://doi.org/10.1016/j.jastp.2015.05.004, 2015.

Russell, J. M., Bailey, S. M., Gordley, L. L., Rusch, D. W., Horányi, M., Hervig, M. E., Thomas, G. E., Randall, C. E., Siskind, D. E., Stevens, M. H., Summers, M. E., Taylor, M. J., Englert, C. R., Espy, P. J., McClintock, W. E., and Merkel, A. W.: The Aeronomy of Ice in the Mesosphere (AIM) mission: Overview and early science results, J. Atmos. Solar-Terrestrial Phys., 71, 289–299, https://doi.org/10.1016/j.jastp.2008.08.011, 2009.

She, C. Y., Berger, U., Yan, Z., Yuan, T., Lübken, F. -J., Krueger, D. A., and Hu, X.: Solar response and long-term trend of midlatitude mesopause region temperature based on 28 years (1990–2017) of Na lidar observations, J. Geophys. Res. Sp. Phys., 124, 7140–7156, https://doi.org/10.1029/2019JA026759, 2019.

Tapping, K. F.: The 10.7 cm solar radio flux (F 10.7), Sp. Weather, 11, 394–406, https://doi.org/10.1002/swe.20064, 2013.

Venkat Ratnam, M., Akhil Raj, S. T., and Qian, L.: Long-Term Trends in the Low-Latitude Middle Atmosphere Temperature and Winds: Observations and WACCM-X Model Simulations, J. Geophys. Res. Sp. Phys., 124, 7320–7331, https://doi.org/10.1029/2019JA026928, 2019.

Wang, N., Qian, L., Yue, J., Wang, W., Mlynczak, M. G., and Russell, J. M.: Climatology of mesosphere and lower thermosphere residual circulations and mesopause height derived from SABER observations, J. Geophys. Res. Atmos., 127, 1–14, https://doi.org/10.1029/2021JD035666, 2022.

Xu, J., Liu, H. L., Yuan, W., Smith, A. K., Roble, R. G., Mertens, C. J., Russell, I. M., and Mlynczak, M. G.: Mesopause structure from Thermosphere, Ionosphere, Mesosphere, Energetics and Dynamics (TIMED/Sounding of the Atmosphere Using Broadband Emission Radiometry (SABER) observations, J. Geophys. Res. Atmos., 112, https://doi.org/10.1029/2006JD007711, 2007.

Yu, W., Garcia, R., Yue, J., Smith, A., Wang, X., Randel, W., Qiao, Z., Zhu, Y., Harvey, V. L., and Tilmes, S.: Mesospheric Temperature and Circulation Response to the Hunga Tonga-Hunga-Ha'apai Volcanic Eruption Journal of Geophysical Research : Atmospheres, 1–10, https://doi.org/10.1029/2023JD039636, 2023.

Yuan, T., Solomon, S. C., She, C. -Y., Krueger, D. A., and Liu, H. -L.: The long-term trends of nocturnal mesopause temperature and altitude revealed by Na lidar observations between 1990 and 2018 at midlatitude, J. Geophys. Res. Atmos., 124, 5970–5980, https://doi.org/10.1029/2018JD029828, 2019.

Yue, J., Russell, J., Jian, Y., Rezac, L., Garcia, R., López-Puertas, M., and Mlynczak, M. G.: Increasing carbon dioxide concentration in the upper atmosphere observed by SABER, Geophys. Res. Lett., 42, 7194–7199, https://doi.org/10.1002/2015GL064696, 2015.

Yue, J., Russell, J., Gan, Q., Wang, T., Rong, P., Garcia, R., and Mlynczak, M.: Increasing water vapor in the stratosphere and mesosphere after 2002, Geophys. Res. Lett., 46, 13452–13460, https://doi.org/10.1029/2019GL084973, 2019a.

Yue, J., Li, T., Qian, L., Lastovicka, J., and Zhang, S.: Introduction to special issue on "Long-term changes and trends in the middle and upper atmosphere," J. Geophys. Res. Sp. Phys., 124, 10360–10364, https://doi.org/10.1029/2019JA027462, 2019b.

Zhang, S., Cnossen, I., Laštovička, J., Elias, A. G., Yue, X., Jacobi, C., Yue, J., Wang, W., Qian, L., and Goncharenko, L.: Long-term geospace climate monitoring, Front. Astron. Sp. Sci., 10, 1–5, https://doi.org/10.3389/fspas.2023.1139230, 2023.

Zhao, X. R., Sheng, Z., Shi, H. Q., Weng, L. B., and Liao, Q. X.: Long-Term Trends and Solar Responses of the Mesopause Temperatures Observed by SABER During the 2002–2019 Period, J. Geophys. Res. Atmos., 125, 1–17, https://doi.org/10.1029/2020JD032418, 2020.

650   Zhao, X. R., Sheng, Z., Shi, H. Q., Weng, L. B., and He, Y.: Middle atmosphere temperature changes derived from

651   SABER observations during 2002-2020, J. Clim., 34, 1, https://doi.org/10.1175/JCLI-D-20-1010.1, 2021.

652